Applied Catalysis B: Environmental 209 (2017) 600–610

Contents lists available at ScienceDirect

Applied Catalysis B: Environmental

journal homepage: www.elsevier.com/locate/apcatb

Effect of transition metals in the hydrogen evolution electrocatalytic activity of molybdenum carbide

Ana M. Gómez–Marín*, Edson A. Ticianelli

Instituto de Química de São Carlos, Universidade de São Paulo, Caixa Postal 780, Fisico Quimica, Av. Trabalhador Sao Carlense, São Carlos, CEP 13560-970, SP, Brazil

ARTICLE INFO

Article history:
Received 31 October 2016
Received in revised form 10 March 2017
Accepted 15 March 2017
Available online 18 March 2017

Keywords:
Electrocatalysis carbides
Sustainable fuels
Transition metals
Metal doping
Electronic effects

ABSTRACT

In this work, the effect of transition metals (TMs), such as Fe, Co, Ni and Cu, on the activity toward the hydrogen evolution reaction (HER) of modified molybdenum carbide (TM-Mo_2C) catalysts has been evaluated. Catalysts were prepared by a temperature programmed reduction method in both an inert and a reductive atmosphere, and characterized by different physicochemical techniques. A high activity toward the HER is measured for all TM-Mo_2C catalysts, with onset potentials lower than −0.06 V, as detected by on-line differential electrochemical mass spectrometry, and mass activities between 29 and 50 mA mg^{-1}, which suggest them as promising non-precious electrocatalysts for this reaction. However, a decrease in the HER activity upon metal doping is measured, following an activity trend of α-Mo_2C > Fe-Mo_2C > Co-Mo_2C > Ni-Mo_2C > Cu-Mo_2C. *In situ* near-edge X-ray adsorption analysis reveals a positive charge of the TM in the materials in the electrochemical environment, at the origin of the deleterious effect of Fe, Co, Ni and Cu, in terms of an electronic effect that modifies the d-electron configuration of α-Mo_2C particles. Additionally, results also suggest that TM-Mo_2C is more stable (lower catalyst dissolution) in acid media than α-Mo_2C. Finally, because there is a catalyst deactivation toward the HER after the α-Mo_2C component of the catalysts is oxidized at $E > 0.7$ V, the oxidation process of α-Mo_2C is employed for estimating, as a first approximation, the number of surface active sites for the HER.

1. Introduction

The global demand for a renewable energy source in a sustainable way has turned the attention toward the electrochemical, or photo-electrochemical, production of hydrogen from water splitting [1,2]. In these processes, the hydrogen evolution reaction (HER), in which aqueous protons in an acid media are reduced to hydrogen by electrons passed through a catalyst is the central reaction. Unfortunately, this reaction is not efficient enough unless a proper catalyst is employed. At present time, platinum (Pt) is the most effective electrocatalyst for the HER [3] but, because it is expensive and scarce, substitute materials have to be developed in order to assure a sustainable hydrogen production.

In the search for new and cheap catalytic materials, Molybdenum-based compounds, such as molybdenum sulfides, MoS_2, and molybdenum carbides, Mo_2C, have been recently demonstrated to be promising candidates as active electrocatalysts for the HER [1,4–15]. However, the catalytic activity of these compounds is still lower than of Pt-based materials and hence, their catalytic activity should be improved in order to be considered as appropriate electrocatalysts for practical applications.

The modification of the electronic and chemical properties of a given material can be effectively reached by the introduction of another element into its lattice, well because of the formation of heteroatom bonds (ligand effect) or owing to the alteration of the average atom–atom bond length (strain effect) [3,16–23]. Inside this approach, transition metal doping of MoS_2 materials with Fe, Co and Ni has demonstrated to improve HER activity of these materials [5,6], while no enhancement has been found when the dopant metal, M^D, was Mn, Cu or Zn metals [6].

In the case of Mo_2C catalysts, the effect of transition metal doping has not been deeply studied. Recently, it has been reported that Fe-doped Mo_2C in acid media is more active towards the HER than pure Mo_2C, while Ni-doped Mo_2C is less active [13]. In contrast, Ni-doped Mo_2C has been found more active than pure Mo_2C in alkaline media [24]. However, comparing the catalytic activity between different materials, from different synthesis procedures, is not an easy task [15]. In this sense, materials prepared by different methods could give rise even to different phases of the same com-

* Corresponding author.
E-mail addresses: amgomezma@iqsc.usp.br, amgomezma@gmail.com (A.M. Gómez–Marín).

http://dx.doi.org/10.1016/j.apcatb.2017.03.044
0926-3373/

pound [25,26], which may guide to contradictory conclusions. In this work, the influence of transition metal (Fe, Co, Ni and Cu) doping in the HER activity of molybdenum carbides is studied. For this, α-Mo_2C and Fe, Co and Ni doped α-Mo_2C materials were prepared by similar temperature programmed carburization procedures and their catalytic activity toward the HER was evaluated under similar conditions.

2. Experimental

2.1. Preparation of transition metal-modified molybdenum carbides

Transition metal-modified molybdenum carbide catalysts, TM-Mo_2C, (TM: Fe, Co, Ni or Cu) were prepared by a carbothermal carburization process consisting in the temperature programmed reduction (TPR) of the different metals on a carbon black substrate (Vulcan XC-72, Cabot Corp., USA) [27–32]. Table 1 resumes the chemical nature and composition of the different employed carbide precursors: MoO_3 (99.5%) and Co_3O_4 (99.5% < 50 nm), Fe_2O_3 (≥99% < 5 μm) or NiO (99.8% < 50 nm); ammonium molybdate ($(NH_4)_6Mo_7O_{24} \times 4H_2O$) and $Fe(CH_3COO)_2$ (95%), $Co(CH_3COO)_2 \times 4H_2O$ (99%) and $Ni(CH_3COO)_2 \times 4H_2O$ (99%), all from Sigma Aldrich [27,28]. In the case of Cu-Mo_2C, only copper nitrate was used as a precursor.

The synthesis procedure consists of three steps: i) Preparation of precursor powders by deposition of metal precursors on the carbon substrate to produce 1 to 1 molar ratio of molybdenum and the corresponding transition metal [33]. ii) Carbothermal reduction of catalyst precursor powders to form the transition metal-modified-Mo_2C; and iii) Passivation of the catalyst surface. The first step was carried out in an ultrasonic bath to form well-dispersed slurries, using isopropanol as solvent. Then, the isopropanol was completely evaporated and solid precursors were dried at 80 °C overnight.

In the second step, the precursor powder, ~200–700 mg, was loaded into a quartz tube, stuffed with quartz wool at the bottom to hold the powders, and its temperature was continuously raised at 1 °C min^{-1} from room temperature (RT) to the final carburization temperature, T_{carb}, and held there for a fixed time, t_h. Carburizations were performed either in an inert (Ar) or a reductive atmosphere (10% H_2/Ar) by employing a Micromeritics 2900 AutoChem II Chemisorption Analyzer Micrometrics, equipped with a thermal conductivity detector (TCD). The progress of carburization of metal oxide precursors was monitored by the TCD signal, interrupting the reaction at different temperatures and analyzing the samples by X-ray diffraction. Preparation conditions for all samples are summarized in Table 2.

In some cases, for comparing the effects both Ar and H_2/Ar-atmospheres, samples were also pre-heated from RT to 550 °C at a heating rate of 20 °C min^{-1} and held there for 30 min in Ar-atmosphere. Then, the temperature was raised at 1 °C min^{-1} to T_{carb}, samples Mo/Ar2 and NiMo/Ar-2, Table 2. The pre-heating step was necessary in order to assure that the carburization in each atmosphere takes place at similar temperatures. However, under these preparation conditions FeMo/Ar-2 and CoMo/Ar-2 gave rise to mixtures of TM-Mo_2C and bimetallic carbides [33]. Also, when T_{carb} in a H_2/Ar-atmosphere is 1000 °C, as the experiences in an Ar-atmosphere, Mo metal is also identified among the crystalline phases in the final products, as reported before [31]. Therefore, these experiences were not included in Table 2.

When the carburization process finalized, the TM-Mo_2C powders were cooled down by quenching at RT and passivated for 1 h in a stream of 2 vol% O_2/He mixture, to prevent further rapid bulk oxidation when samples are exposed to air. Additionally, in order to evaluate the stability of metal-modified α-Mo_2C catalysts in acid media and remove any free metallic species in the products, some samples were treated in boiling 1 M HCl for 2 h (acid treated TM-Mo_2C catalysts). This acid treatment can be also considered as an accelerated degradation test, chosen instead of common lengthy-stability tests, which usually consist in galvanostatic or potentiostatic electrolysis for several days, and that frequently are not enough to determine measurable differences in the catalytic activity when comparing two different materials.

2.2. Catalyst characterization

The diffraction patterns of TM-Mo_2C catalysts were measured by X-ray diffraction (XRD, RIGAKU model RU200B) in the 2θ range from 20 to 80° and using CuKα radiation. Peaks were identified on the basis of the Joint Committee on Power Diffraction Standards (JCPDS) files and references [4,10,13,31]. In this sense, α-Mo_2C corresponds to the hexagonal structure of Mo_2C. The crystallite size of products was established from XRD data using the Debye-Scherrer equation, $D_c = 0.9\lambda/(\beta \cos\theta)$, where λ is the wavelength of the X-ray radiation (λ = 1.541 Å), β is the width of the peak at half-maximum and θ is the Bragg angle. The 2–3 major peaks were used in calculations, which for α-Mo_2C phase (JCPDS 35-0787) correspond to the {101}, {002} and {100} planes, yielding similar values of D_c [29,30,32].

Scanning electron microscopy (SEM) images were performed on a LEO, 440 SEM-EDX system (Leica-Zeiss, DSM-960) and on a FEG JEOL JSM 7500F. Approximate chemical compositions of as prepared samples were estimated by energy dispersive X-ray spectroscopy (EDX, Isis System Series 300) with a microanalyzer (Link analytical QX 2000) and a Si (Li) detector, using a 20 keV incident electron beam., and reported data are the average of, at least five measurements taken from different region of the samples. Transmission electron microscopy (TEM) images were performed on a JOEL 2100 transmission electron microscope at 200 kV.

The X-ray absorption spectroscopy (XAS) measurements were undertaken at the SXS beam line at the National Synchrotron Light Laboratory (LNLS), Brazil, at the XAS beam line (D08 B XAFS2) [34].

Table 1
Composition of carbide precursors for different TM-α-Mo_2C samples.

Catalysts	Mo Precursor	wt.% Mo Precursor	TM Precursor	wt.% Metal Precursor	wt.% Vulcan Carbon black
Mo/H_2	MoO_3	77.2	–	–	22.8
$CoMo/H_2$	MoO_3	51.4	Co_3O_4	28.7	19.9
$NiMo/H_2$	MoO_3	53.3	NiO	27.5	19.2
$FeMo/H_2$	MoO_3	51.0	Fe_2O_3	28.5	20.5
Mo/Ar	$(NH_4)_6Mo_7O_{24} \times 4H_2O$	65.0	–	–	35.0
CoMo/Ar	$(NH_4)_6Mo_7O_{24} \times 4H_2O$	28.6	$Co(CH_3COO)_2 \times 4H_2O$	40.2	31.2
FeMo/Ar	$(NH_4)_6Mo_7O_{24} \times 4H_2O$	32.5	$Fe(CH_3COO)_2$	32.1	35.4
NiMo/Ar	$(NH_4)_6Mo_7O_{24} \times 4H_2O$	28.6	$Ni(CH_3COO)_2 \times 4H_2O$	40.2	31.2
CuMo/Ar	$(NH_4)_6Mo_7O_{24} \times 4H_2O$	30.3	$Cu(NO_3)_2$	38.3	31.4
Mo/Ar-2	MoO_3	77.3	–	–	22.7
NiMo/Ar-2	MoO_3	53.3	NiO	27.5	19.2

Table 2
Carburization conditions and main Mo-crystalline phases, identified by XRD, of different TM-α-Mo_2C samples.

Catalysts	Carburization gas	T_{carb} (°C)	Holding time, t_h (min)	Crystalline phases	Crystallite size (nm)[a]
CoMo/H_2	10% H_2-Ar	625	30	Co-α-Mo_2C	29
NiMo/H_2	10% H_2-Ar	625	30	Ni-α-Mo_2C	35
FeMo/H_2	10% H_2-Ar	625	30	Fe-α-Mo_2C, MoO_2,	42
FeMo/H_2-2	10% H_2-Ar	725	30	Fe-α-Mo_2C	39
Mo/H_2	10% H_2-Ar	625	30	MoO_2	30
Mo/H_2-2	10% H_2-Ar	725	30	α-Mo_2C	29
Mo/Ar	Ar	1000	0	α-Mo_2C	40
CoMo/Ar	Ar	1000	0	Co-α-Mo_2C	52
FeMo/Ar	Ar	1000	0	Fe-α-Mo_2C	42
NiMo/Ar	Ar	1000	0	Ni-α-Mo_2C	42
CuMo/Ar	Ar	1000	0	Cu-α-Mo_2C	41
Mo/Ar-2	Ar	750	20	α-Mo_2C	35
NiMo/Ar-2	Ar	765	30	Ni-α-Mo_2C	40

[a] Calculated from XRD data.

In situ XAS results were obtained in the transmission mode and in the near-edge (XANES) region of the Fe K (7112 eV) and Cu K (8979 eV) edges to evaluate the electronic structures of Fe and Cu atoms on the catalysts in the electrochemical environment, by using a homemade spectroelectrochemical cell [35]. Working electrodes consisted of pellets formed with dispersed catalysts mixed with a Nafion® solution (Sigma–Aldrich, 6 wt.%). The reference electrode was a saturated Ag/AgCl and the counter electrode consisted in a Pt sheet. Nevertheless, all potentials in the text are referenced to the potential of the Reversible Hydrogen Electrode (RHE), $E^0_{H_2/H^+}$ = –222 mV vs Ag/AgCl, sat. KCl. Data treatment was performed with the Athena program [36].

2.3. Electrochemical measurements

Electrochemical measurements were conducted at RT, ~22 °C, in a two–compartment, three electrodes, all–glass cell, using an Autolab (Nova) equipped with an interchangeable rotating disk electrode setup (Pine Instruments). Suprapure perchloric acid (Merck) was used to prepare aqueous solutions in ultrapure water (Purelab Ultra, Elga–Vivendi). H_2 and Ar (N50, Air Liquid) were also employed. Potentials were measured against the RHE and a large Au plaque was used as a counter electrode. Similar results were also measured when a Pt plaque, instead of the Au plaque, was used as a counter electrode. Ohmic drop corrections were made when necessary, to compensate the electrolyte resistance.

Glassy carbon disks (5 mm diam., 0.196 cm^2), polished to a mirror finish (0.05 μm alumina, Buehler) before each experiment, served as substrate for TM-Mo_2C catalysts. Electrodes were prepared by pipetting onto the glassy carbon surface an aliquot of the ultrasonically redispersed catalyst ink. The inks were prepared by suspending in isopropanol by ultrasound certain amount of the as prepared TM-Mo_2C powders to form a suspension (~1 to 2 mg mL^{-1}). After evaporation of isopropanol from the glassy carbon surface, an aliquot of a diluted Nafion® solution (Aldrich) was dropped on top of the dried catalyst powder and let it to dry in air atmosphere to fix the electrocatalyst, giving Nafion® films of thickness ~ 0.1 μm.

Directly after preparation, the electrodes were immersed into deaerated, 0.1 M $HClO_4$ electrolyte. Initially, as a cleaning procedure for the catalyst surface, the electrode potential was cycled several times between −0.2 to 0.2, or 0.4, V. The upper potential limit, E_{up}, was chosen to be lower than the open circuit potential of the electrode, in order to avoid extensive catalyst oxidation (see below). The activity of TM-Mo_2C catalysts toward the hydrogen evolution reaction (HER) was evaluated in H_2-free and H_2-saturated solutions, different to the solution in which the cleaning procedure was performed, in quiescent solutions and rotating electrodes. Current densities either were normalized by the geometric area of the glassy carbon substrate or to the electrochemically active surface area (ESA) of TM-Mo_2C catalysts, estimated from the integrated charge of the irreversible oxidation peak attributed to Mo_2C species, as explained below, or double layer capacitance measurements.

With respect to HER measurements, it should be noted that i) reported currents correspond to the steady state currents reached after the cleaning procedure was performed. ii) the glassy carbon RDE and pure Vulcan carbon (VC), at similar loadings to those used in TM-Mo_2C catalyst experiments, did not show any appreciable hydrogen production activity at potentials positive of −0.3 V, in agreement with Ref. [37]. Thus, the overall activity of Vulcan carbon present in TM-Mo_2C catalysts and the glassy carbon RDE can be considered negligible in the evaluated potential range in this work.

2.4. Differential electrochemical mass spectrometry (DEMS) setup

On-line DEMS measurements were performed with a Pfeiffer Vacuum QMA 200 quadrupole mass spectrometer using a setup consisting of two differentially pumping chambers. More details of this method can be found in Ref. [37] and [38,40]. The technique allows the on-line detection of volatile and gaseous products of electrochemical reactions during the application of a potential scan. The electrochemical cell was constructed according to previous published principles [37,39,40]. Experimentally, current-potential profiles were simultaneously recorded with mass intensity *versus* potential curves, for selected values of mass/charge (m/z) ionic signals: H_2 evolution was monitored at m/z = 2, while the electrochemical oxidation of α-Mo_2C was followed at m/z = 28 (CO) and m/z = 44 (CO_2). The electrode potential was cycled at 0.01 V s^{-1} between either 0.4–0.2 V, for HER polarization curves, or 0.05–1.2 V, for the electrochemical oxidation of the samples.

Working electrodes were prepared in the form of a thin film by pipetting onto a gold layer (1.13 cm^2 area, 50 nm thickness), obtained by Au sputtering onto a Gore-Tex® PTFE membrane (pore size 0.02 μm), an aliquot of the ultrasonically redispersed catalyst ink (~4.0–5.0 mg mL^{-1}, 20 μL of Nafion® solution–5 wt.%.). After the evaporation of the alcohol at ambient temperature, the electrodes were washed with ultrapure water and inserted in the electrochemical cell.

3. Results and discussion

3.1. Catalyst synthesis and characterization

Although the exact reaction mechanism during the carburization is still unknown, the TPR process for MoO_3 by carbon to produce Mo_2C has been well investigated before [27–29,31,32].

Experiments have shown that the heating rate, the final TPR temperature, the gas atmosphere (reductive or inert) and the type of carbon source, among other factors may determine the global composition of the final product [13,28–31,42–44]. Therefore, in this work, preparation procedures of TM-Mo_2C catalysts were determined based on previous works [27–29,31,32] and by running preliminary synthesis from different precursors and in both inert and reductive atmospheres. For Fe and Co, only acetate precursors give pure Fe- or Co-Mo_2C samples in an inert atmosphere for the precursor composition evaluated here. Lower amounts of initial carbon give as a final material a mixture of Fe- or Co-Mo_2C and bimetallic carbides, Fe_3Mo_3C or Co_3Mo_3C/Co_6Mo_6C.

Once prepared, catalysts were characterized by XRD and EDX measurements. XRD diffraction patterns for some TM-Mo_2C catalysts are given in Fig. 1, and the main crystalline phases of final products are resumed in Table 2. For Mo/Ar-2 and NiMo/Ar-2 XRD patterns after the acid treatment with 1 M HCl are also given, curve 3. In all samples, but not FeMo/H_2 (curve 2), the major crystalline phase is the stable hexagonal α-Mo_2C (JCPDS 35-0787), together with nano-crystalline transition metal particles, crystallite size ~42, 52, 41 and 43 nm, in TM-Mo_2C catalysts: Co (JCPDS 01-1255), Fe (JCPDS 65–4899), Ni (JCPDS 01-1260) and Cu (JCPDS 85–1326), respectively. All XRD peaks in Fig. 1 are slightly shifted, ~±0.1°, in relation to the XRD peaks in α-Mo_2C carbide (Table S1). This fact may be ascribed not only to changes in lattice parameters, occurring when a metal is inserted onto the lattice, but also to strain effects on a macroscopic scale of the material, *i.e.* systematic stacking and twin faults, point defects, among others [41].

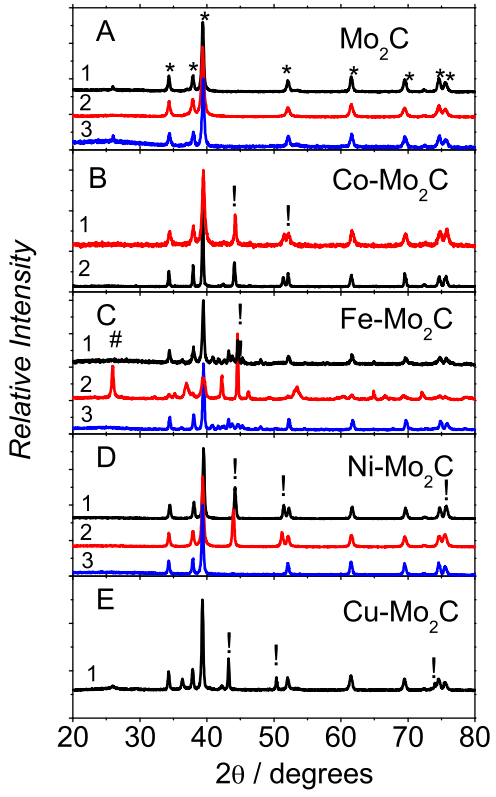

Fig. 1. XRD Patterns of synthesized TM-Mo_2C catalysts. Identified crystalline phases: (*) α-Mo_2C (JCPDS 35-0787), (#) MoO_2 (JCPDS 01-0615), (!) Metallic element: Co (JCPDS 01-1255), Fe (JCPDS 65-4899), Ni (JCPDS 01-1260) and Cu (JCPDS 85-1326). Curves 1 and 2 are XRD patterns from catalysts prepared in Ar and H_2/Ar atmospheres, respectively. Curve 3 in C corresponds to the XRD of FeMo/H_2-2, while in A and D it is the XRD after the acid treatment of Mo/Ar-2 and NiMo/Ar-2, respectively.

For all TM-Mo_2C, excepting Fe-Mo_2C, no differences in XRD patterns are found for TM-Mo_2C prepared in Ar or 10% H_2/Ar atmospheres, even for those samples prepared at high T_{carb} (1000 °C), and only an increase in the crystallite size is calculated, Table 2. In the case of Fe-Mo_2C catalysts, it was not possible to prepare a pure Fe-Mo_2C sample. In the best case, synthesized samples include trace amounts of bimetallic carbide: Fe_3Mo_3C (JCPDS 47–1191) and/or $Mo_{12}Fe_{22}C_{10}$ (JCPDS 39-0825). In contrast to these results, a recent work reports pure bimetallic carbides as the only final products after carburization at 950 °C [33], instead of the TM-Mo_2C catalysts mixtures obtained here, *i.e.* pure transition metal + α-Mo_2C. The different carbon source employed during the synthesis could be the origin of this difference in the final composition in both studies [42–45].

In addition, no peaks corresponding to metallic Mo were detected in any of the samples, and only Mo/H_2-2 exhibits traces of MoO_2 (JCPDS 01-0615), Fig. 1A. This fact suggests that the presence of transition metals during the carburization process of MoO_3, in a reductive atmosphere, promotes the formation of α-Mo_2C, as suggested before for the direct reduction of MoO_3 to molybdenum carbides by a reacting mixture of CH_4/$4H_2$ [46]. This is especially evident for CoMo/H_2 and NiMo/H_2 for which pure TM-Mo_2C is obtained at 625 °C, while for FeMo/H_2 a mixture of Fe-Mo_2C and MoO_2 is produced. In contrast, for Mo/H_2, only MoO_2 is identified under the same conditions and a higher T_{carb} (725 °C) is needed to obtain α-Mo_2C as the main crystalline phase, Table 2. Nevertheless, Mo/H_2-2 sample has one of the lowest crystallite size, together with CoMo/H_2, calculated from XRD data, despite it was not produced at the lowest T_{carb}, Table 2. This indicates that transition metals also favor crystallite size growth of α-Mo_2C, similar to what has been reported in past works for the synthesis of WC catalysts [47].

EDX data of catalysts prepared in an Ar-atmosphere (Table S2) were obtained by averaging data from at least three different regions of each material. Analysis reveal good homogeneities only for samples synthesized from low amount of carbon in the precursor, as seen by the standard deviations, besides a Transition Metal/Molybdenum molar ration (TM/Mo) higher than 1.0, the nominal metal content, for CoMo/Ar and NiMo/Ar-2 (before the acid treatment), which could indicated partial sublimation of MoO_3 during the carburization [8,28]. However, because no MoO_3 sublimation was observed by thermogravimetry/differential thermal measurements during the carburization of carbon-supported ammonium molybdate samples [8], the high TM/Mo ratios might simply reflect the presence of free metallic particles inside the samples, giving rise to certain sample inhomogeneity. In contrast, neither SEM images nor EDX maps (Figs. S1–S4 in Supplementary material) suggest sample inhomogeneity at micrometer scale. In this sense, EDX results show a complete overlap of the TM-Mo_2C catalyst constituents, which implies a homogeneous distribution in all samples at a micrometer scale.

Similarly, high resolution SEM images for the NiMo/Ar-2 catalyst, upper images in Fig. 2, do not reveal any sample inhomogeneity at a ~100 nm scale and only suggest an increase in the particle size and a change in morphology after the acid treatment, lower images Fig. 2, indicating a lost in surface area in this latter case. Sample inhomogeneity in the catalyst, *i.e.* pure transition metal + α-Mo_2C, is only evident at nanometric scale, from punctual EDX measurements from high resolution SEM images before (Fig. S5 in Supplementary material) and after (Fig. S6 in Supplementary material) the acid treatment. In this case, the initial sample is composed by metallic particles in addition to Ni-Mo_2C particles, while after the acid treatment the composition of the samples appears quite homogenous and only particles with similar composition are found.

After the acid treatment, EDX measurements reveal the removal of free metallic particles from NiMo/Ar-2, although a small portion

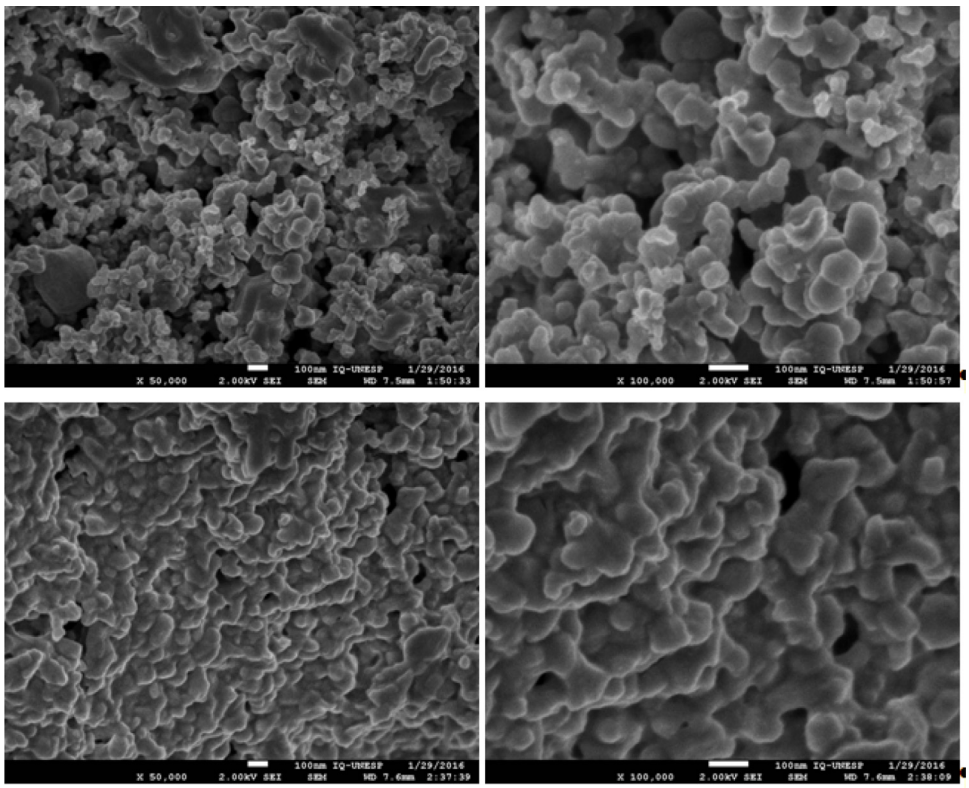

Fig. 2. High resolution SEM images of Ni-Mo_2C before (upper figures) and after (lower figures) the acid treatment.

of metallic Ni still remains (Table S2 and Fig. S6 in Supplementary material). In contrast, the XRD pattern for this catalyst only reveals the presence of α-Mo_2C, Curve 3 in Fig. 1D. This may suggest that either the size of free metallic Ni particles is too small to be detected by XRD or they are amorphous or they are inside the lattice of the α-Mo_2C and cannot be washed out by HCl. In addition, the Carbon/Molybdenum molar ration (C/Mo) for both NiMo/Ar-2 and Mo/Ar-2 also decreases after washing them with HCl, which also indicates a "cleaning" of the particles by removing part of excess carbon on the carbides, deposited during carburization at temperatures higher than ∼650 °C [29,30,48]. In agreement, TEM images of Mo/Ar, CoMo/Ar and NiMo/Ar show the TM-Mo_2C particles surrounded by a carbon layer, Fig. 3.

In situ X-ray absorption near edge structure (XANES) measurements in the electrochemical environment, at the open circuit potential (OCP) of the catalysts, were also performed to verify that transition metals inside the TM-Mo_2C catalysts were not leached out to the solution under the electrochemical environment. Fig. 4 shows *in situ* XANES spectra for FeMo/Ar (A) and CuMo/Ar (B) at 0.34 and 0.45 V vs. RHE, respectively, in a 0.1 M $HClO_4$. The OCP for α-Mo_2C in the same solution is ∼0.45 V. As it can be seen, XANES spectra confirm that both metals, Fe and Cu, remain inside the catalyst in the acid media, even at potentials higher than the standard potential for dissolution of each pure metal: −0.44 and 0.34 V vs. RHE. Besides, it is expected that at lower potentials than the OCP, no extra metal dissolution takes place. Nevertheless, the amount of metal inside each catalyst may be lower than the initial composition of catalysts because of a partial dissolution.

XANES is a powerful technique that provides specific information about the valence structure of an element inside a compound. In this sense, qualitative information about the oxidation state of a metal inside a catalyst can be obtained by comparing its XANES spectrum against XANES spectra of standard materials: the absorption edge generally blue shifts as the metal center becomes more oxidized. For the Fe-Mo_2C catalyst, the intermediate white line intensity, and an intermediate intensity of the characteristic metallic bump of the edge-step in the XANES spectrum of the Fe K-edge suggests both Fe^{2+}, as in FeO, and metallic Fe features present inside the catalyst, Fig. 4A. Additionally, because the structure observed above the maximum in absorbance in a XANES spectrum results from multiple-scattering processes [49], the strongly damped signal in the XANES spectrum of Fe-Mo_2C could suggest an amorphous structure of the Fe, in agreement with the lack of metallic XRD peaks after the acid treatment.

In contrast, the weak pre-edge feature at 8976.3 eV in the XANES spectrum of the Cu K-edge for Cu-Mo_2C catalyst (inset to Fig. 4B), and an edge position at 8988.2 eV, calculated as the energy at the maximum of the first derivative at the XANES region, suggest a Cu^{2+} state inside this catalyst [50]. In addition, the edge position and the intensity of the feature at the maximum absorption at 8992.8 eV also suggest the presence of water ligands in the first coordination shell of the metal [50,51]. Similar to what has been reported in the XANES spectrum of hydrated $Cu(NO_3)_2$ [51], because the absorption maxima above the edge are due to multiple scattering and their intensity and position are dependent on the local geometric structure of the material rather than on the electronic structure [50].

The fact that M^D bears a non-zero charge and that Cu inside the catalyst has a higher oxidation state than the Fe, is rather unexpected. Due to the necessity of an electronic equilibrium in interfaces [52], the alignment of the band structure of two separate metals would require a charge transfer from the metal with lower work function, ϕ: Mo 4.30 eV [53], or Mo_2C 3.85 eV [54], to the metal with higher ϕ: Fe 4.65 eV, or Cu 4.7 eV [53]. Of course the charge states and the electronic structures of TM-Mo_2C catalysts are far from being explained just by differences in ϕ, and they should largely be influenced by the carbon inside the lattice, ϕ = 5.0 [55], the carbon support and the electrochemical environ-

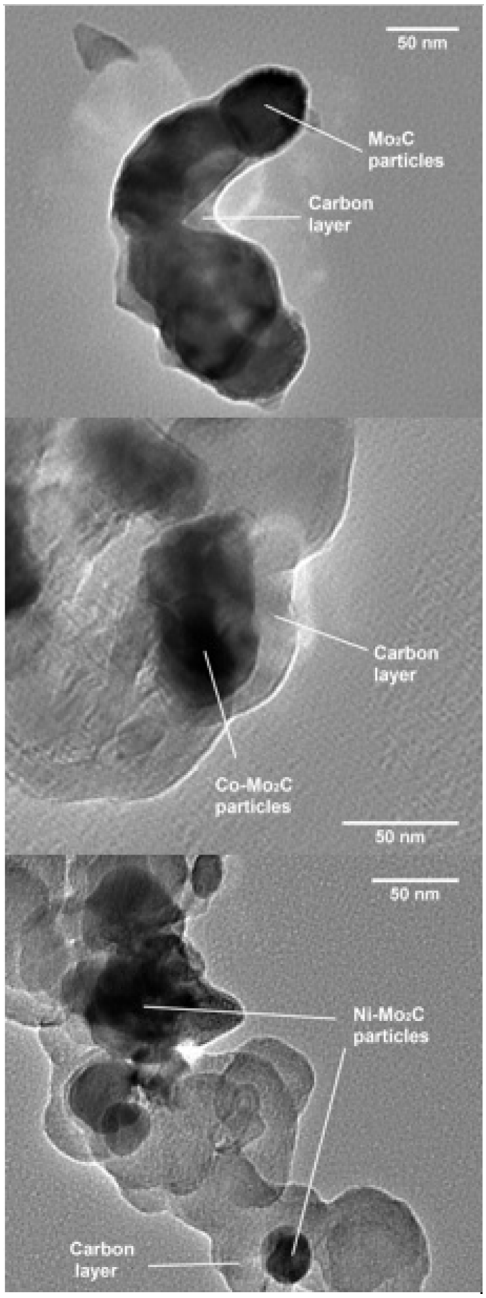

Fig. 3. TEM images of α-Mo_2C (top), Co-Mo_2C (middle) and Ni-Mo_2C (bottom).

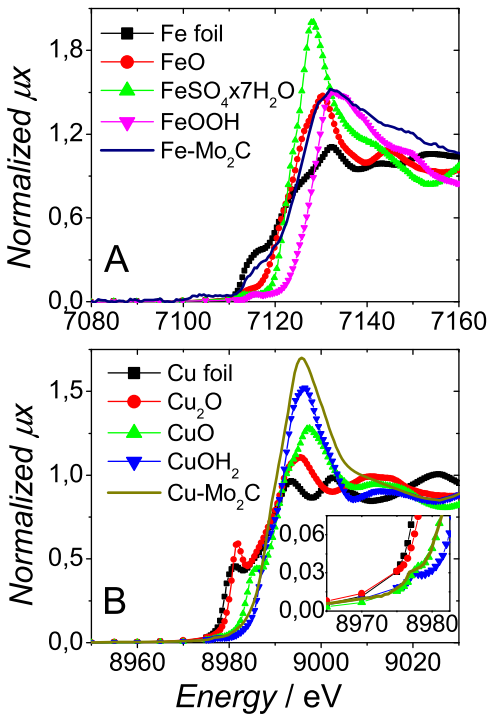

Fig. 4. *In situ* XANES spectra of Fe-Mo_2C (A) and Cu-Mo_2C (B) at the open circuit potential 0.34 and 0.45 V vs. RHE, respectively, in a 0.1 M $HClO_4$ solution.

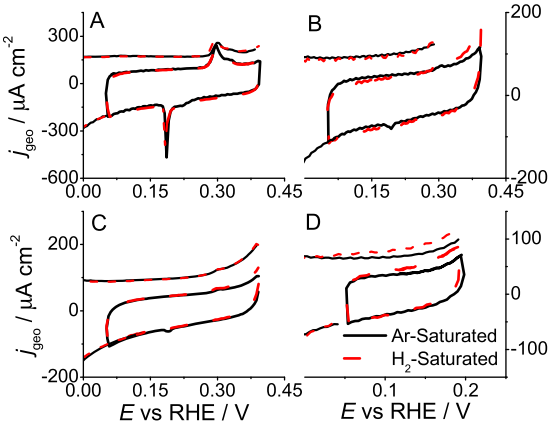

Fig. 5. Stable cyclic voltammograms of Mo/Ar-2 (A), CoMo/Ar (B), FeMo/Ar (C) and NiMo/Ar-2 (D) catalysts in Ar- (solid) and H_2-saturated (dashed) 0.1 $HClO_4$. Scan rate 0.05 V s^{-1}. Thin lines are CVs with −0.2 V as the lower potential limit.

ment. However, giving the dependence of the HER activity on ϕ [53], and specifically on the valence state of Mo atoms in α-Mo_2C [8,16–18,56], the insertion of a doping cation into the lattice will certainly modify its reactivity toward the HER, as discussed below.

3.2. Electrochemical characterization of TM-Mo_2C catalysts

Stable cyclic voltammograms (CVs) of TM-Mo_2C powders, regardless the synthesis conditions, in Ar and H_2-saturated 0.1 M $HClO_4$ solutions are featureless between $0.0 < E < 0.4$ V, Fig. 5, and only the α-Mo_2C catalyst displays a clear redox process at ∼0.3 V in the positive-going scan, Fig. 5A. However, because this feature is absent in the CV after the acid treatment (Fig. S7 in Supplementary material), it might be concluded that surface oxides and/or amorphous molybdenum oxides residual from the carburization process may be responsible for this redox process [7,57–59].

Similarly to what has been reported before [60,61], no or little difference in current densities are observed between Ar- and H_2-saturated CVs for all TM-Mo_2C carbides in Fig. 5, even in CVs taken at slower scan rates (data not shown). This fact, besides the low current increase in the $0.0 < E < 0.4$ V potential region after potential excursions to low potentials where the HER takes places, $E < -0.15$ V, coming from oxidation of the H_2 around the catalyst surface, suggests a poor catalytic activity toward the hydrogen oxidation reaction (HOR), in agreement with reported works [62–64]. In this sense, to highlight this low activity, CVs in Fig. 5 are shown only for potentials above 0.0 V, although curves were experimentally taken at two different lower potential limits, E_{down}: 0.05 V (thicker lines) and −0.2 V (thinner lines). The upper potential limit, E_{up}, in this figure was chosen to be 0.4 V vs. RHE, because at higher potentials the oxidation of TM-Mo_2C catalysts takes place [15,65–67].

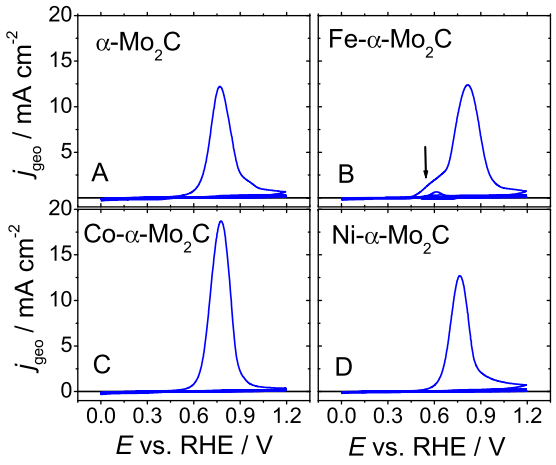

Fig. 6. Cyclic voltammograms in Ar-saturated 0.1 $HClO_4$ of the oxidation of Mo/H_2-2 (A), $CoMo/H_2$ (B), $FeMo/H_2$-2 (C) and $NiMo/H_2$ (D). Scan rate 0.05 V s^{-1}.

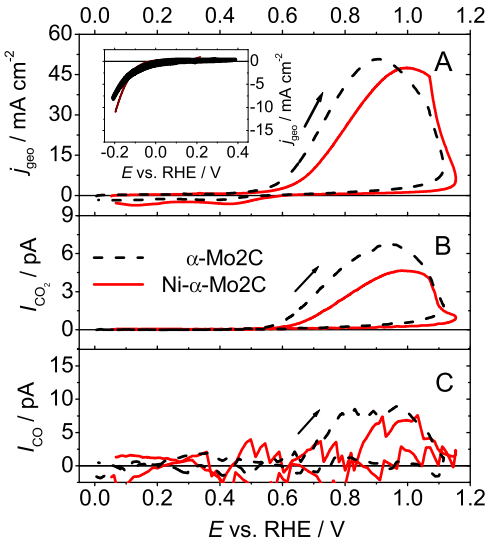

Fig. 7. Simultaneous recorded polarization curves (A) and mass spectrometric cyclic voltamograms for $m/z = 44$, CO_2, (B), and $m/z = 28$, CO (C) for the first (solid line) oxidation cycle of $NiMo/H_2$ in Ar-saturated 0.1 M $HClO_4$. Inset to (A): HER polarization curves before (thin) and after the first (solid-thick) catalyst's oxidation cycle. Scan rate 0.01 V s^{-1}. Current densities were calculated by employing the electrode geometric area. For the sake of comparison, similar curves for Mo/H_2-2 are also given (dashed lines) [15].

At potentials higher than those depicted in Fig. 5, a sudden increase in current during the first positive-going scan indicates corrosion of all samples, Fig. 6. During the immediate negative-going scan, some reduction features around ~0.2–0.4 V appear in the CVs, probably arising from the reduction of molybdenum species formed during the oxidation of carbides [57,65–67]. In the second positive-going excursion to high potentials, peak currents of all oxidation steps of TM-Mo_2C catalysts noticeably decrease, Fig. 6. Additionally, a markedly decrease in the HER catalytic activity evaluated on these oxidized catalysts is measured (see below). After oxidation of the samples, resulting CVs display a lower current density than non-oxidized samples, which could be a result of either a lower conductivity of oxidized samples, as expected if molybdenum oxides are the oxidized product [57], or a decrease in the amount of material deposited in the electrode.

From Fig. 6, it is clear that all TM-Mo_2C catalysts follow an electrochemical oxidation process comparable to the process of α-Mo_2C catalyst and only a small shift in the potential of the peak current is registered. In this sense, for a better understanding of the electro-oxidation process of TM-Mo_2C, DEMS measurements were simultaneously performed during the oxidation of $NiMo/H_2$ to determine gas compounds formed, and compared both oxidation processes, Fig. 7. It is seen that, similar to the process of Mo/H_2-2 [15], the electrochemical oxidation of $NiMo/H_2$ also involves the simultaneous oxidation of both molybdenum, Mo, and carbon, C, atoms, although in this case the beginning of the oxidation is slightly shifted toward higher potentials, $E > 0.6$ V, and the amounts of CO_2 and CO produced are lower. Additionally, the potential at which CO production begins is also shifted, suggesting a higher oxidation rate for the CO_2 production.

The electrochemical response of TM-Mo_2C catalysts, at least qualitatively, do not depend on the atmosphere employed during their synthesis, but the final phase obtained, and similar CVs to those depicted in Fig. 6 are also recorded for the catalysts prepared in an Ar atmosphere. In this regards, it is important to highlight that only for Fe-Mo_2C a small shoulder before the main oxidation peak is also recorded in the CVs (arrow in Fig. 6B). Because this shoulder becomes a peak when the amount of bimetallic carbide in the sample increases, this electrochemical signal can be ascribed to the electrochemical response of the traces of Fe-Mo bimetallic carbide in the sample, revealed by XRD data (Fig. 1). This finding strongly suggests that cyclic voltammetry is a sensitive technique to assess the purity not only of a molybdenum carbide sample, as highlighted before [15], but also for bimetallic samples, as in our case. This issue will be discussed in detail elsewhere.

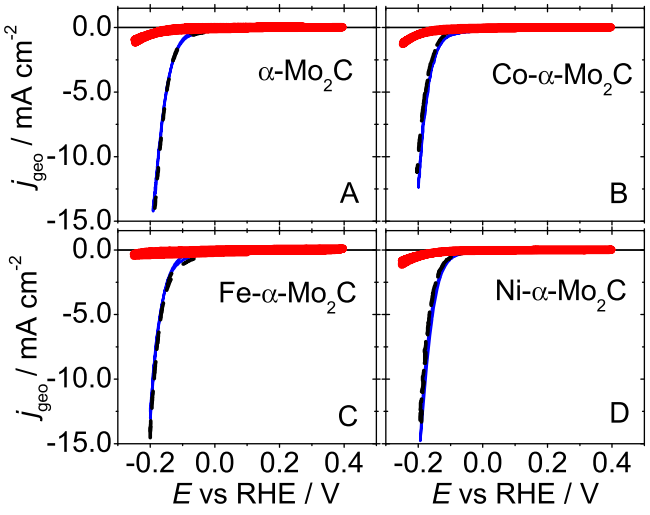

Fig. 8. Initial polarization curves (dashed line), and after 1000 cycles (thin solid line), for the HER of TM-Mo_2C catalysts in Ar-saturated 0.1 $HClO_4$. Scan rate 0.05 V s^{-1}. Curves after the electrochemical oxidation of the catalysts are also given (thick solid line).

3.3. *Electrocatalytic activities of TM-Mo_2C toward HER*

The TM-Mo_2C catalysts were also systematically investigated regarding the effect of transition metals doping in the reactivity of Mo_2C for the HER. Fig. 8 displays the stable polarization curves of TM-Mo_2C catalysts, synthesized in a reductive atmosphere, for HER in Ar-saturated 0.1 $HClO_4$. Similar curves are also obtained at lower scan rates, in H_2-saturated solutions and at different rotation rates. Initially, activities are higher than those depicted in Fig. 8 for all TM-Mo_2C catalysts, but in subsequent scans, within the same potential window, there is a decrease in activity, until CVs become stable. This is most likely due to the instability in acid media of molybdenum oxides, present in all samples as surface oxides and/or residual from the carburization process, which introduces an extra reduction current in first scans at negative potentials.

All curves in Fig. 8 evidence a high HER activity for all TM-Mo_2C, with stable reduction currents only related of H_2 formation, without any other faradaic processes occurring at the electrode surface, and low onset potentials of ~−0.06 V for NiMo/H_2 and ~−0.05 V for Mo/H_2-2 [15], as confirmed from DEMS measurements (Fig. S9 in Supplementary material). Therefore, all these materials can be considered a promising non-precious HER electrocatalysts, especially taking into account their electrochemical stability under HER conditions in acidic media [68], Figs. 6 and 7. Indeed, reaction onsets for TM-Mo_2C carbides are even lower than those reported for other similar α-Mo_2C materials: −0.333 V [69], −0.244 V [4], −0.100 V [7], −0.070 [14] and −0.062 V [1] and, therefore, they also have a remarkable activity among Mo_2C-based catalysts.

Compared with pure metals, the overall HER performance of TM-Mo_2C materials is also comparable, an even better in some cases, than the one displayed by HER active non-noble metals [53]. This is because most of these metals corrode in the acid environment and their catalytic activity cannot be sustained for a long time at potentials higher than the standard potential for metal dissolution [70]. In this sense, for example, although Ni metal can be considered a good HER catalyst in acid electrolytes [53], with a low HER reaction onset, ~0.084 V, and cathodic current densities of ~−10 mA cm^{-2} at −210 mV under certain conditions [70,71], no stable HER currents can be sustained above ~−0.257 V vs RHE, its standard dissolution potential. In contrast, all TM-Mo_2C catalysts in Fig. 8 are stable in the whole HER potential range and exhibit lower reaction onsets and higher stable current densities, >20 mA cm^{-2}, before the dissolution potential of Ni metal is reached.

Only when samples are cycled at high potentials TM-Mo_2C catalysts oxidize in the first scan in the positive-going direction, as depicted in Fig. 6, and HER activities measured in the following negative-going scan drop for all materials, Fig. 8. Furthermore, because in the second positive-going scan to high potentials the oxidation peak almost disappears for all samples, Fig. 6, the loss in HER activities in all TM-Mo_2C catalysts can be attributed to the electrochemical oxidation of the materials, similar to the reported before for α-Mo_2C [15]. Similar deactivation in the HER activity immediate after catalyst oxidation has been reported for MoS_2 and WS_2 based catalysts [5]. For thick catalyst's layers, as that one employed for performing DEMS measurements, inset to Fig. 7A, the loss in HER activity is lower than the loss reported in Fig. 8, because an incomplete catalyst's usage [15].

3.4. Effect of doping in the activity of Mo_2C toward the HER

To compare catalyst's performance between different materials, kinetic parameters, such as exchange current densities, j_0, Tafel slopes, mass activities, $MA_{E=-Er}$, and current densities, $j_{E=-Er}$, at a reference potential, E_r, are usually determined. Fig. 9 resumes polarization curves, Fig. 9A, and current densities at 0.18 V, $j_{E=-0.18\,V}$, Fig. 9B, of all TM-Mo_2C samples, calculated by employing the electrode geometric area. For the sake of comparison, polarization curves for 20% commercial Pt/C nanoparticles and MoO_2/C, sample Mo/H_2 in Table 2, are also given.

From Fig. 9, it is observed that, in contrast to TM-Mo_2C catalysts, MoO_2/C cannot be considered as an HER catalyst in the depicted potential range, in agreement with what has been reported by previous studies [7,72]. Similarly, it has also been found that neither MoO_3 nor intermediate Molybdneum bronze oxides are active materials for HER [72], which explains why, after the catalyst's electrooxidation, all materials decrease their HER activity. Therefore, although the surface of TM-Mo_2C catalysts may be oxidized under HER conditions [15,25], the presence of molybdenum carbide species, maybe as molybdenum oxycarbide, is necessary to the HER activity depicted in Figs. 8 and 9, as already suggested in previous studies [7,15,25]. Nevertheless, the exact chemical nature responsible of the HER activity is still unknown. This is because, although the main component of all catalysts is α-Mo_2C carbide, the true surface composition under the electrochemical reaction environment of all samples is unknown, and it can be quite different to the bulk composition of the catalysts, characterized by ex-situ techniques.

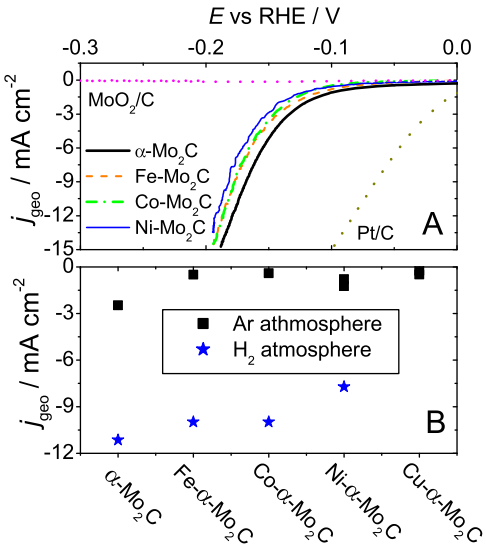

Fig. 9. Polarization curves (A) and current densities at 0.18 V„ (B) for α-Mo_2C and TM-Mo_2C catalysts, prepared in a 10% H_2/Ar atmosphere, in Ar-saturated 0.1 $HClO_4$. Scan rate 0.01 V s^{-1}. For the sake of comparison, polarization curves for 20% commercial Pt/C (Pt-Etek) and MoO_2 and current densities for the catalysts prepared in an Ar-atmosphere are also given in Figs. A and B, respectively. Current densities were calculated by employing the geometric electrode area.

In addition, although HER activities in Fig. 9 are similar for all TM-Mo_2C carbides, they are lower than the one for α-Mo_2C, prepared under the same atmosphere. Therefore, it is clear that the addition of TMs into the α-Mo_2C lattice decreases its catalytic activity toward the HER and the activity trend decreases as we move to the right side of the periodic table: α-Mo_2C > Fe-Mo_2C > Co-Mo_2C > Ni-Mo_2C > Cu-Mo_2C. Similarly, mass activities at 0.15 V, $MA_{E=-0.15\,V}$, for catalysts in Fig. 9A are 50.2 > 39.2 > 35.7 > 29.1 mA mg^{-1} for α-Mo_2C, Fe-Mo_2C, Co-Mo_2C and Ni-Mo_2C, respectively, which are found to be between reported values for carbon supported Mo_2C materials, *i.e.* $MA_{E=-0.15\,V}$ ~0.7 to 95 mA mg^{-1} [1,7,8,10].

The deleterious effect of metal doping on the HER activity of TM-Mo_2C catalysts can be understood considering the strong H_2 binding energy, ΔE_H, of Mo metal and the volcano-type relationship between ΔE_H and HER activity [2,3], that predicts an increase (decrease) in the activity for a weaker (stronger) ΔE_H on Mo atoms. Therefore, because of the inverse relation in carbon-supported Mo_2C materials between positively charged Mo atoms and the position of the d-band center, ε_d, [17,18], an increase in the positive charge on Mo atoms would lower ε_d, [17,18] weakening ΔE_H on Mo atoms [56], as recently suggested [8]. Hence, the HER activity of α-Mo_2C catalysts decreases upon metal doping because of the positive charge of the M^D inside the lattice, as evidenced by XANES data in Fig. 4, which would reduce the net positive charge over Mo atoms in the material. In this framework, the smaller (larger) M^D charge of Fe (Cu) atoms would produce the smaller (larger) reduction on the HER activity on Fe(Cu)-Mo_2C, explicating the activity trend in Fig. 9.

According to theoretical studies, the modification of the electronic and chemical properties of a given material upon metal doping can be mainly explained as the resultant of two different effects: ligand and strain effects [3,18–23], although other effects such as ensemble effects and bifunctional mechanisms [17,18,20]

can also occur. In our case, the compressive strain into the lattice of α-Mo_2C due to metal doping, because of the lower atomic size of the TMs evaluated here relative to Mo atoms, would result in a broadening and lowering of the energy of the d-band [3,18–23] and thus, an increase in the HER activity. Therefore, the fact that TM-Mo_2C carbides have a lower HER activity than α-Mo_2C strongly suggests that ligand effects, represented by charge transfer of the dopant metal to adjacent atoms, dominate over strain effects [17], a non-surprising result taking into account that interactions between early (mid) and late transition metals are seen to be strong [23].

Considering a recent study in transition metal oxides (TMOs) in which their surface reactivity has been tuned by inserting/removing surface oxygen vacancies into the structure, because of the change in the density of coordinatively unsaturated metal cations (M_{CUS}) [22], it appears that the reactivity of transition metal carbides, TMC, and TMOs is controlled by similar phenomena. Additional support for this idea comes from the fact that results in Fig. 9 can be also explained by considering the effective orbital radius, r_d, of the host, r_d^{MH}, and doping, r_d^{MD}, metals, as predicted for the change in reactivity in doped 4d and 5d late transition metals dioxides,TMO_2s [21]. Inside this framework, a more exothermic adsorption energy is expected if $r_d^{MH} > r_d^{MD}$, explaining the activity trend α-Mo_2C > Fe-Mo_2C > Co-Mo_2C > Ni-Mo_2C > Cu-Mo_2C because of $r_d^{Mo} > r_d^{Fe} > r_d^{Co} > r_d^{Ni} > r_d^{Cu}$ [73].

The similarities between the factors that control the reactivity of TMCs and TMOs can be understood in light of the strong correlation between the states near the Fermi level and adsorption energies for TMC [16,56] and TMO_2s, [22]. It suggests a complex relation between ε_d and the electrocatalytic activity for non-uniform systems where ε_d can be affected by more than one factor [16,21,22,56], instead of a direct correlation between ε_d and adsorption energies, as typically assumed [20,56]. In addition, the apparent correspondence between TMCs and TMOs reactivity, may suggest some strategies for improving the HER activity of α-Mo_2C, through a proper tuning of the density of M_{CUS}. This can be achieved well by inserting carbon vacancies into their surface [56], or by metal doping of α-Mo_2C with a M^D with an r_d comparable to, or slightly greater than r_d^{Mo}, such as Sc, W or Nb metals [73]. Progress in our laboratory is currently realized to confirm or denied this hypothesis.

Contrarily to Fig. 9 a higher HER activity for Fe-Mo_2C than for α-Mo_2C, despite a positive charge on Fe atoms, has been recently reported [13]. However, in this case, measured HER activities are significantly smaller than in Fig. 9B, with $j_{E=-0.18\,V} < 1.0$ and <2.1 mA cm^{-2} for Mo_2C and Fe-Mo_2C, respectively, and the increase in activity suitably correlates with the amount of graphitic carbon in Fe-Mo_2C materials. Hence, the improved activity could be better explained in light of the catalytic activity of encapsulate Fe into graphitic carbon toward the HER [74], rather to a doping effect. The appearance of a peak at 9.3 eV in the valence band of Fe-Mo_2C, close to the core-level binding energy for C 2p (~9.0 eV) [20], once a small amount Fe was doped into de lattice of the material clearly supports this hypothesis [13]. Indeed, results here may explain the lower HER activity of Ni-Mo_2C catalysts in Ref [13], for which less graphitic carbon relative to α-Mo_2C was measured.

3.5. Calculating the specific activity of TM-Mo_2C catalysts

A look to results in Fig. 9B suggest that, apparently, HER activities of the catalysts prepared in an Ar-atmosphere are significantly lower than those ones of the carbides prepared in a H_2/Ar atmosphere, although the HER activity trend for both synthesis procedures is the same. However, as already highlighted [15], when comparing the intrinsic catalyst's performance toward a reaction, measured currents have to be first normalized by the electrochemically surface area (ESA) of the material, instead of using the geometric electrode surface as in Fig. 9B. Therefore, before of comparing the HER activity of synthesized catalysts in both the Ar- and H_2/Ar-atmospheres, intrinsic j_0's, together to Tafel slopes, of TM-Mo_2C are calculated by employing the ESA and given in Fig. 10.

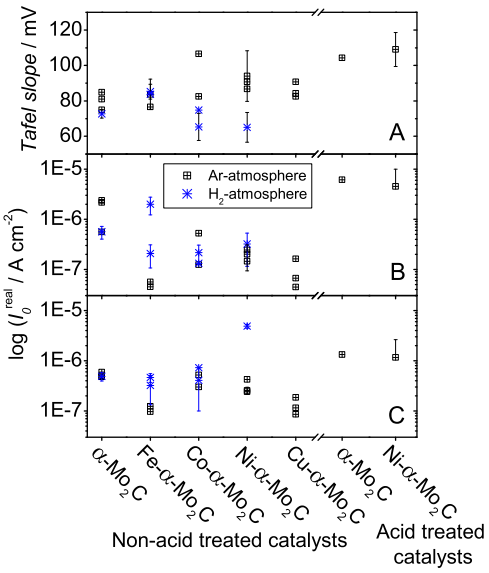

Fig. 10. Tafel slopes (A) and exchange currents for the HER of TM-Mo_2C normalized by the electrochemical surface area calculated by employed either (B) the integrated charge of the oxidation process or double layer capacitance measurements (C), assuming a specific double layer capacitance of 40 μF cm^{-2} for all TM-Mo_2C materials [75,76].

In calculating j_0's, the ESA of each catalyst was determined by two methods [15]. The first one used the integrated charge of the irreversible oxidation peak in Fig. 6, because its direct correlation to the HER activity, considering16 transferred electrons in the process [15,65–67] and a charge density of bulk α-Mo_2C of 204 μC cm^{-2} [13,77]. Analogous to the method for estimating the active sites in MoS_2 and WS_2-based catalysts [5,75]. The second one employed double layer (DL) capacitance, C_{dl}, measurements, assuming a specific C_{dl}, $C^{spe}{}_{dl}$, of 40 μF cm^{-2} for all TM-Mo_2C catalysts [75,76], because of the same order of magnitude of $C^{spe}{}_{dl}$ for many metallic and semiconducting materials [78]. Here, C_{dl}'s of the catalysts were determined as charging current densities at $E = 0.15$ V divided by the scan rate, ν, from CVs at different ν's, in a potential range of 0.05–0.4 V (Fig. S10 in Supplementary material), in which no faradaic processes are observed [52].

Contrarily to Fig. 9B, Fig. 10B and C clearly evidence that j_0's for each TM-Mo_2C synthesized in either an Ar- or H_2/Ar atmosphere are similar, and j_0's decrease upon metal doping, following the same activity trend reported in Fig. 9. Therefore, differences in 's in Fig. 9B, should be attributed to a particle size effect [8,17], Table 2, and/or differences in the morphology of the catalysts [12], rather to actual differences in the intrinsic catalytic activity. In addition, because both employed methods of normalizing j_0's provide comparable values for all catalysts, within the same order of magnitude, results in Fig. 10B and C also suggests that the use of the electrochemical oxidation process of TM-Mo_2C to estimate the ESA of these materials can be a suitable method, as good as capacitance measurements. The largest deviation found is for Fe-Mo_2C catalyst, which contains traces amount of bimetallic carbide.

In analyzing the catalyst's electroactivity, Tafel slopes also play an important role, because they can provide information about not only the possible rate-determining step (RDS) in whole reaction mechanism but also concerning the electron transport inside the materials [8,14,79]. According to previous reports [2,11,80]. Tafel slopes of 120, 40 and 30 mV dec^{-1} are expected for the HER reaction

when the RDS is the electrochemical adsorption of H_{ads} from H^+ (Volmer step [81]), the electrochemical desorption of H_{ads} to form H_2 (Heyrovsky step [82]) or the non-electrochemical desorption of H_{ads} to form H_2 (Tafel step [83]), respectively.

For TM-Mo_2C materials in Fig. 10A, Tafel slopes are found among 65–110 mV, suggesting the occurrence of a Volmer-Heyrovsky mechanism, with the adsorption of H_{ads} as the RDS. However, a close look into this figure evidences that, in general, higher Tafel slopes are calculated for those catalysts synthesized in an Ar-atmosphere, despite the same j_0's values. Therefore, more than a change in the RDS, differences in Tafel slopes between materials should be interpreted in terms of differences in the electron transfer inside the catalyst [14,15,79]. The latter may occur because of a higher amount of amorphous oxides, residual from the carburization process [59], in the catalysts synthesized in an inert atmosphere than in those ones synthesized in a reductive atmosphere, which would reduce the intrinsic electron conductivity of these samples [15], due to the semiconducting nature of molybdenum oxides [79]. Similar differences in Tafel slopes have been also reported for bulk Mo_2C, ~78–98 mV [8,10,14] and carbon supported Mo_2C materials, ~54–72 mV [1,7,8,10,14].

3.6. Stability of TM-Mo_2C catalysts in acid media

Stability in acid media is an important issue for a HER catalysts for practical applications, like proton electrolyte membrane electrolyzers. In this regard, all TM-Mo_2C catalysts are stable and practically maintain the same catalytic HER activity reported above, even after sweeping them for more than 1000 cycles between −0.2 to 0.4 V, Fig. 8. Additionally, in order to evaluate the long-term stability, Mo/Ar-2 and NiMo/Ar-2 samples were treated in hot 1 M HCl for 2 h. Tafel slopes and exchange current densities for these samples are also given in Fig. 10. From this figure, increased Tafel slope and intrinsic activities of the samples after the acid treatment are clear, although their mass activities significantly decrease, ~5.2 to 11.5 mA mg^{-1}, respectively.

The increase in j_0 toward the HER in acid-treated samples can be explained in terms of a catalyst's cleaning, described above. On the other hand, the decrease in $MA_{E=-0.15\,V}$ can be understood considering a loss in the ESA, that has been evidenced in a small oxidized peak during the first scan to high potentials after the acid treatment (Fig. S11 in Supplementary material). It is possible that this reduction in area occurred because of catalyst's dissolution, catalyst's agglomeration, Fig. 2, and/or catalyst's oxidation. The latter possibility would also explain the increase in Tafel slopes, in terms of a decrease in the intrinsic electron conductivity of the samples. Nonetheless, the fact that $MA_{E=-0.15\,V}$ after the acid treatment is higher for NiMo/Ar-2 than Mo/Ar-2, while the opposite occurs before the acid treatment, suggests that doping α-Mo_2C with TMs increases the stability in acid media toward catalyst dissolution, in agreement to what has been published before for Fe-Mo_2C [13].

4. Conclusions

In this work, transition metal (Fe, Co, Ni and Cu)-modified Mo_2C catalysts were prepared by temperature programmed carburization in inert and reductive atmospheres and characterized by XRD, SEM-EDX, XANES, DEMS and cyclic voltammetry. The activity of TM-Mo_2C catalysts toward the hydrogen evolution reaction (HER) and their stability in acid were measured. Results show that all catalysts irreversibly oxidize at high positive potentials and this process can be used to estimate the electrochemical active surface area. It is found that while metal doping increases the acid and electrochemical stability of α-Mo_2C catalysts, it slightly decreases their catalytic HER activity. The deleterious effect of Fe, Co, Ni and Cu doping has been explained in terms of an electronic effect, represented in a charge transfer of the dopant metal to adjacent atoms, that modifies the d-electron configuration of α-Mo_2C particles. Nevertheless, polarization curves of all TM-Mo_2C evidence a high activity toward the reaction, suggesting them as promising, non-precious, HER electrocatalysts.

Acknowledgments

The authors would like to thank Fundação de Amparo a Pesquisa do Estado de São Paulo (FAPESP – Procs. 2013/16930-7 and 2014/23486-9), Brazil, for financial supports and the Brazilian Synchrotron Light Laboratory (LNLS), where XAS measurements were performed.

Appendix A. Supplementary data

Supplementary data associated with this article can be found, in the online version, at http://dx.doi.org/10.1016/j.apcatb.2017.03.044.

References

[1] D.H. Youn, S. Han, J.Y. Kim, J.Y. Kim, H. Park, S.H. Choi, J.S. Lee, ACS Nano 8 (2014) 5164–5173.
[2] Y. Zheng, Y. Jiao, M.K. Jaroniec, S.Z. Qiao, Angew. Chem. Int. Ed. 54 (2015) 52–65.
[3] J.K. Nørskov, T. Bligaard, A. Logadottir, J.R. Kitchin, J.G. Chen, S. Pandelov, U. Stimming, J. Electrochem. Soc. 152 (2005) J23–J26.
[4] Y.N. Regmi, G.R. Waetzig, K.D. Duffee, S.M. Schmuecker, J.M. Thode, B.M. Leonard, J. Mater. Chem. A 3 (2015) 10085–10091.
[5] J. Bonde, P.G. Moses, T.F. Jaramillo, J.K. Nørskov, I. Chorkendorff, Faraday Discuss. 140 (2008) 219–231.
[6] D. Merki, H. Vrubel, L. Rovelli, S. Fierro, X. Hu, Chem. Sci. 3 (2012) 2515–2525.
[7] H. Vrubel, X. Hu, Angew. Chem. 124 (2012) 12875–12878.
[8] W.-F. Chen, C.-H. Wang, K. Sasaki, N. Marinkovic, W. Xu, J.T. Muckerman, Y. Zhu, R.R. Adzic, Energy Environ. Sci. 6 (2013) 943–951.
[9] R. Michalsky, Y.-J. Zhang, A.A. Peterson, ACS Catal. 4 (2014) 1274–1278.
[10] K. Zhang, Y. Zhao, D. Fu, Y. Chen, J. Mater. Chem. A 3 (2015) 5783–5788.
[11] B. Sljukic, M. Vujkovic, L. Amaral, D.M.F. Santos, R.P. Rocha, C.A.C. Sequeira, J.L. Figueiredo, J. Mater. Chem. A 3 (2015) 15505–15512.
[12] C. Ge, P. Jiang, W. Cui, Z.H. Pu, Z. Xing, A.M. Asiri, A.Y. Obaid, X. Sun, J. Tian, Electrochim. Acta 134 (2014) 182–186.
[13] C. Wan, B.M. Leonard, Chem. Mater. 27 (2015) 4281–4288.
[14] L. Liao, S. Wang, J. Xiao, X. Bian, Y. Zhang, M.D. Scanlon, X. Hu, Y. Tang, B. Liu, H.H. Girault, Energy Environ. Sci. 7 (2014) 387–392.
[15] A.M. Gómez-Marín, E.A. Ticianelli, Electrochim. Acta 220 (2016) 363–372.
[16] A. Vojvodic, A. Hellman, C. Ruberto, B.I. Lundqvist, Phys. Rev. Lett. 103 (2009) 146103-1-4.
[17] P. Liu, J.A. Rodriguez, J. Chem. Phys. 120 (2004) 5414–5423.
[18] P. Liu, J.A. Rodriguez, J.T. Muckerman, J. Phys. Chem. B 108 (2004) 15662–15670.
[19] C. Tsai, K. Chan, J.K. Nørskov, F. Abild-Pedersen, Catal. Sci. Technol. 5 (2015) 246–253.
[20] M.T. Gorzkowski, A. Lewera, J. Phys. Chem. C 119 (2015) 18389–18395.
[21] Z. Xu, J.R. Kitchin, J. Chem. Phys. 142 (2015), 104703-1–104703-9.
[22] H.B. Tao, L. Fang, J. Chen, H.B. Yang, J. Gao, J. Miao, S. Chen, B. Liu, J. Am. Chem. Soc. 138 (2016) 9978–9985.
[23] J.R. Kitchin, J.K. Nørskov, M.A. Barteau, J.G. Chen, J. Chem. Phys. 120 (2004) 10240–10246.
[24] K. Xiong, L. Li, L. Zhang, W. Ding, L. Peng, Y. Wang, S. Chen, S. Tan, Z. Wei, J. Mater. Chem. A 3 (2015) 1863–1867.
[25] C. Wan, Y.N. Regmi, B.M. Leonard, Angew. Chem. Int. Ed. 53 (2014) 6407–6410.
[26] A.M. Gómez-Marín, J.L. Bott-Neto, J.B. Souza, T.L. Silva, W. Beck, L. Varanda, E.A. Ticianelli, ChemElectroChem 3 (2016) 1570–1579.
[27] S. Chaudhury, S.K. Mukerjee, V.N. Vaidya, V. Venugopal, J. Alloys Compd. 261 (1997) 105–113.
[28] Z. Hang-Yu, L. Zheng-Bang, Y. Hai-Seen, L. Lin-Gen, J. Iron Steel Res. Int. 20 (2013) 51–56.
[29] J.S. Lee, S.T. Oyama, M. Boudart, J. Catal. 106 (1988) 125–133.
[30] J.S. Lee, L. Vope, F.H. Ribeiro, M. Boudart, J. Catal. 112 (1988) 44–53.
[31] R. Guil-López, E. Nieto, J.A. Botas, J.L.G. Fierro, J. Solid State Chem. 190 (2012) 285–295.
[32] A. Hanif, T. Xiao, A.P.E. York, J. Sloan, M.L.H. Green, Chem. Mater. 14 (2002) 1009–1015.
[33] Y.N. Regmi, B.M. Leonard, Chem. Mater. 26 (2014) 2609–2616.
[34] M. Abbate, F.C. Vicentin, V. Compagnon-Cailhol, M.C. Rocha, H. Tolentino, J. Synchrotron Radiat. 6 (1999) 964–972.

[35] J. McBreen, W.E. O'Grady, K.I. Pandya, R.W. Hoffman, D.E. Sayers, Langmuir 3 (1987) 428–433.
[36] B. Ravel, M. Newville, J. Synchrotron Radiat. 12 (2005) 537–541.
[37] S.T. Hunt, T.M. Kokumai, D. Zanchet, Y. Romaní-Leshkov, J. Phys. Chem. C 119 (2015) 13691–13699.
[38] J.P.I. de Souza, S.L. Queiroz, F.C. Nart, Quim. Nova. 23 (2000) 384–391.
[39] B. Bittins-Cattaneo, E. Cattaneo, P. Konigshoven, W. Vielstich, A.J. Bard (Eds.), Electroanalytical Chemistry –A Series of Advances, Marcel Dekker, New York, 1991.
[40] R. Ianniello, V.M. Schmidt, Ber. Bunsenges, Phys. Chem. 99 (1995) 83–86.
[41] B.D. Cullity, Elements of X-ray Diffraction, 2nd ed., Addison-Wesley, 1978.
[42] S. Li, W.B. Kim, J.S. Lee, Chem. Mater. 10 (1998) 1853–1862.
[43] T. Wang, Q. Luo, Y.-W. Li, J. Wang, M. Beller, H. Jiao, Appl. Catal. A: Gen. 478 (2014) 146–156.
[44] T. Wang, X. Liu, S. Wang, C. Huo, Y.-W. Li, J. Wang, H. Jiao, J. Phys. Chem. C 115 (2011) 22360–22368.
[45] H.J. Guzmán, W. Xu, D. Stacchiola, G. Vitale, C.E. Scott, J.A. Rodríguez, P. Pereira-Almao, Can. J. Chem. 91 (2013) 573–582.
[46] K.T. Jung, W.B. Kim, C.H. Rhee, J.S. Lee, Chem. Mater. 16 (2004) 307–314.
[47] E.J. Rees, C.D.A. Brady, G.T. Burstein, Mater. Lett. 62 (2008) 1–3.
[48] Y.C. Kimmel, D.V. Esposito, R.W. Birkmire, J.G. Chen, Int. J. Hydrogen Energy 37 (2012) 3019–3024.
[49] G. Long, J.D. Hautot, Q.A. Pankhurst, D. Vandormael, F. Grandjean, J.P. Gaspard, V. Briois, T. Hyeon, K.S. Suslick, Phys. Rev. B. 57 (1998) 10716–10722.
[50] E.M.C. Alayon, M. Nachtegaal, E. Kleymenov, J.A. van Bokhoven, Microporous Mesoporous Mater. 166 (2013) 131–136.
[51] N. Cheng, Y.-L. Wei, Y.-W. Yang, J.-F. Lee, Phys. Scr. T115 (2005) 907–908.
[52] A.J. Bard, L.R. Faulkner, Electrochemical Methods: Fundamentals and Applications, 2nd ed., John Wiley and Sons, New York, 2001.
[53] S. Trasatti, J. Electroanal. Chem. Interfacial Electrochem. 39 (1972) 163–184.
[54] V.S. Fomenko, G.V. Samsonov (Eds.), Handbook of Thermionic Properties, Plenum Press, 1966.
[55] D.R. Lide (Ed.), CRC Handbook of Chemistry and Physics, 84th ed., CRC Press, Boca Raton, FL, 2003 (Section 12, p 124).
[56] R. Michalsky, Y.-J. Zhang, A.J. Medford, A.A. Peterson, J. Phys. Chem. C 118 (2014) 13026–13034.
[57] V.S. Saji, C.-W. Lee, ChemSusChem 5 (2012) 1146–1161.
[58] Z. Chen, D. Cummins, B.N. Reinecke, E. Clark, M.K. Sunkara, T.F. Jaramillo, Nano Lett. 11 (2011) 4168–4175.
[59] J.S. Choi, J.M. Kraft, A. Krzton, G. Djéga-Mariadassou, Catal. Lett. 81 (2002) 175–180.
[60] M. Nagai, M. Yoshida, H. Tominaga, Electrochim. Acta 52 (2007) 5430–5436.
[61] S. Izhar, M. Yoshida, M. Nagai, Electrochim. Acta 54 (2009) 1255–1262.
[62] S. Izhar, S. Otsuka, M. Nagai, J. New Mater. Electrochem. Syst. 11 (2008) 15–20.
[63] C.J. Barnett, G.T. Burstein, A.R.J. Kucernak, K.R. Williams, Electrochim. Acta 42 (1996) 2381–2388.
[64] T. Kudo, G. Kawamura, H. Okamoto, J. Electrochem. Soc. 130 (1983) 1491–1497.
[65] L.A. Il'icheva, M.Kh. Freid, V.A. Suprunov, N.A. Tyurina, Sov. Powder Metall. Met. Ceram. 17 (1978) 594–598.
[66] L.A. Il'icheva, L.N. Frolova, M.Kh. Freid, V.A. Suprunov, Sov. Powder Metall. Met. Ceram. 14 (1975) 916–920.
[67] R.D. Armstrong, A.F. Douglas, J. Appl. Electrochem. 2 (1972) 143–149.
[68] M.C. Weidman, D.V. Esposito, Y.-C. Hsu, J.G. Chen, J. Power Sources 202 (2012) 11–17.
[69] S. Wirth, F. Harnisch, M. Weinmann, U. Schröder, Appl. Catal. B: Environ. 126 (2012) 225–230.
[70] J. Lu, T. Xiong, W. Zhou, L. Yang, Z. Tang, S. Chen, ACS Appl. Mater. Interfaces 8 (2016) 5065–5069.
[71] J. Tamm, L. Tamm, J. Arol'd, Russ. J. Electrochem. 40 (2004) 1152–1155.
[72] D.P. Summers, S. Leach, K.W.J. Frese, J. Electroanal. Chem. 205 (1986) 219–232.
[73] W.A. Harrison, S. Froyen, Phys. Rev. B 21 (1980) 3214–3221.
[74] J. Deng, P. Ren, D. Deng, L. Yu, F. Yang, X. Bao, Energy Environ. Sci. 7 (2014) 1919–1923.
[75] J.D. Benck, Z. Chen, L.Y. Kuritzky, A.J. Forman, T.F. Jaramillo, ACS Catal. 2 (2012) 1916–1923.
[76] E. Frackowiak, F. Beguin, Carbon 39 (2001) 937–950.
[77] J.R. Kitchin, J.K. Nørskov, M.A. Barteau, J.G. Chen, Catal. Today 105 (2005) 66–73.
[78] B.E. Conway, V. Birss, J. Wojtowicz, J. Power Sources. 66 (1997) 1–14.
[79] H. Vrubel, T. Moehl, M. Grätzel, X. Hu, Chem. Commun. 49 (2013) 8985–8987.
[80] S.A. Vilekar, I. Fishtik, R. Datta, J. Electrochem. Soc. 157 (2010) B1040–B1050.
[81] T. Erdey-Gruz, M. Vomer, Z. Phys. Chem. Abt. A 150 (1930) 203–213.
[82] J. Heyrovsky, Recl. Trav. Chim. Pays-Bas 46 (1927) 582–585.
[83] J. Tafel, Z. Phys. Chem. 50 (1905) 641–712.